Held, S., Schill, E., Pavez, M., Díaz, D., Muñoz, G., Morata, D., Kohl, T. (2016): Resistivity distribution from mid-crustal conductor to near-surface across the 1200 km long Liquiñe-Ofqui Fault System, southern Chile. - *Geophysical Journal International*, *207*, 3, pp. 1387—1400.

DOI: http://doi.org/10.1093/gji/ggw338

Geophysical Journal International

Geophys. J. Int. (2016) **207,** 1387–1400
Advance Access publication 2016 September 12
GJI Geodynamics and tectonics

doi: 10.1093/gji/ggw338

Resistivity distribution from mid-crustal conductor to near-surface across the 1200 km long Liquiñe-Ofqui Fault System, southern Chile

Sebastian Held,[1] Eva Schill,[2] Maximiliano Pavez,[3,4] Daniel Díaz,[3,4] Gerard Muñoz,[5] Diego Morata[4,6] and Thomas Kohl[1]

[1] *Institute of Applied Geosciences, Karlsruhe Institute of Technology (KIT), Karlsruhe, Germany. E-mail: sebastian.held@kit.edu*
[2] *Institute for Nuclear Waste Disposal, Karlsruhe Institute of Technology (KIT), Karlsruhe, Germany*
[3] *Department of Geophysics, Facultad de Ciencias Físicas y Matemáticas, Universidad de Chile, Santiago, Chile*
[4] *Andean Geothermal Center of Excellence (CEGA), Universidad de Chile, Santiago, Chile*
[5] *German Research Centre for Geosciences (GFZ), Potsdam, Germany*
[6] *Department of Geology, Facultad de Ciencias Físicas y Matemáticas, Universidad de Chile, Santiago, Chile*

Accepted 2016 September 10. Received 2016 September 6; in original form 2016 July 3

SUMMARY

Mid-crustal conductors are a common phenomenon in magnetotelluric studies. In the Andean Cordillera of southern Chile, they appear to concentrate along major fault zones. A high-resolution, broad-band magnetotelluric survey including 31 stations has been carried out along two profiles perpendicular to (1) the Liquiñe-Ofqui Fault Systems (LOFS) and (2) the Villarrica-Quetrupillán-Lanín volcanic lineament running parallel to the Mocha-Villarrica Fault Zone (MVFZ). The survey aimed at tracing one of the known conductors from mid-crustal depth to near-surface along these faults. Directionality and dimensionality were analysed using tensor decomposition. Phase tensors and induction arrows reveal two major geoelectric strike directions following the strike of LOFS and MVFZ**.** 2-D inversion shows low resistivity zones along both fault systems down to a depth of >10 km, where the brittle-ductile transition is expected. Along the LOFS, the two anomalies are linked to (1) Lake Caburgua, where the LOFS broadens to about 2 km of lateral extension and seems to represent a pull-apart structure, and (2) the intersection with the Villarrica-Quetrupillán-Lanín volcanic lineament, where seismic activity was observed during the latest eruption in March 2015. A connection of the mid-crustal conductor to the ESE-WNW-striking fault zones is indicated from the presented data.

Key words: Magnetotellurics; Hydrothermal systems; Volcanic arc processes; Dynamics and mechanics of faulting; South America.

1 INTRODUCTION

Geodynamic processes on different scales such as deformation along major fault zones, formation of major geothermal fields or deposition of ore minerals in faults are connected to thermal fluids in the Earth's crust and often characterized by high electrical conductivity zones. While thermal conductivity structures revealed by abnormal heat flow pattern are limited to small variations (e.g. Kohl & Rybach 1996), the dynamics of electric resistivity, covering several orders of magnitudes compared to typical crustal rock, characterize mid-crustal conductors (e.g. Unsworth *et al*. 2004; Hill *et al*. 2009; Wannamaker *et al*. 2014). The origin of these electric conductors has early been attributed to graphite (Frost *et al*. 1989; Jödicke 1992). More recently, links to aqueous fluids and secondary minerals in fault zones (Korja *et al*. 2008; Brasse *et al*. 2009; Weckmann *et al*. 2012), to partial melt (Unsworth *et al*. 2005; Hill *et al*. 2009), and to metamorphic processes (Wannamaker *et al*. 2014; Zhang *et al*. 2015) have been discussed.

Worldwide, it is observed that these conductors have an upper depth limit near the brittle-ductile transition (Jones 1992; Jiracek 1995). The North and East Anatolian Fault Systems, for example, are both characterized by a broad low resistivity zone at mid-crustal depth that extends into the lower crust to depths below 10 km (Türkoğlu *et al*. 2015). At the San Andreas Fault lateral variation in resistivity seems to be related to active deformation mechanisms. At Parkfield, where a transition of the fault from a creeping to a locked section occurs, a superficial conductor to a depth of 2–3 km is observed (Unsworth *et al*. 1997). A connection between this zone and a mid-crustal conductor is proposed by Becken *et al*. (2008). A small fault-zone conductor was observed on the locked Carrizo segment (Mackie *et al*. 1997; Unsworth *et al*. 1999). The conductor extends to mid-crustal depths at Hollister where creeping movement on the faults are observed (Bedrosian 2002).

In the compressional tectonic setting of the Southern Alps, a crustal conductor at 30–40 km depth has been attributed to fluids from prograde metamorphism within a thickening crust

(Wannamaker *et al*. 2002). Interestingly, the conductor rises northwest toward the trace of the Alpine Fault and continues to vertical orientation near surface. This is attributed to fluids ascending across the brittle-ductile transition approaching the surface through induced hydro-fractures. Shallow extensions of the deep highly conductive features are coincident with modern, hydrothermal veining and gold mineralization interpreted to originate from the deep crust.

Although mid-crustal conductors in southern Chile occur close to deep-rooted major fault zones (Brasse & Soyer 2001; Kapinos *et al*. 2016), a prolongation through the brittle ductile transition is not evident from long-period magnetotelluric (MT) data (Brasse *et al*. 2009). Broad-band MT survey including period ranges down to 1000 s in geothermal fields however, often show also a link between high conductivities and major fault zones down to about 7–8 km depth (e.g. Rowland & Sibson 2004; Geiermann & Schill 2010; Spichak *et al*. 2015).The relevance of fluid pathways from mid-crustal electric and thermal anomalies along fault zones is most evident in the Himalayan arc and the Tibetan plateau where large-scale strike-slip fault pattern (e.g. Schill *et al*. 2004) allow for regionally significant advective heat transport (Hochstein & Regenauer-Lieb 1998).

In the framework of a joint German–Chilean geothermal research project, the electric resistivity of the Villarrica area, located in the volcanic arc of southern Chile, was investigated on reservoir scale. Low interstation-distance, broad-band MT measurements were closely linked to the existing long-period data along an E–W profile across the Liquiñe-Ofqui Fault Systems (LOFS). LOFS is intersected by a secondary major fault zone striking ESE–WNW and offsetting the LOFS by a few kilometres in the study area (Rosenau *et al*. 2006). Therefore, a second profile has been acquired sub-perpendicular to this structure.

2 GEOLOGICAL SETTING

Villarrica Volcano (39°25′S, 71°56′W) and its two neighbouring volcanoes Quetrupillán and Lanín, are major Holocene stratovolcanoes formed by the subduction of the Nazca- below the South America Plate. The Nazca Plate converges with a velocity of 7–9 cm a^{-1} (Norabuena 1998; Angermann *et al*. 1999), at an oblique direction of approx. N78°E (Somoza 1998) and with a dip of 25–30° (Barazangi & Isacks 1976) against the South America Plate forming the Andean Cordillera on the western margin of South America. Initiated in Jurassic times, subduction occurred mainly under a compressional tectonic regime with an extensional interval between Eocene and Miocene times (Parda-Casas & Molnar 1987; Melnick & Echtler 2006). The recent stress pattern is characterized by maximal horizontal stress trending N60°E and subhorizontal minimal stress (Lavenu & Cembrano 1999; Rosenau *et al*. 2006). The trench is located 260 km west of the study area, whereas the subducted Nazca Plate lies at a depth of about 120 km below Mt. Villarrica (Krawczyk *et al*. 2006).

In south-central Chile, the Andean Cordillera overlies a thinned crust (Hildreth & Moorbath 1988). Between the subduction of the Juan Fernandez Ridge (33°S) and the Chile Triple Junction (46°S) major stratovolcanoes occur along the so-called Southern Volcanic Zone in the Andean Cordillera (Stern 2004). Volcanic centres are often located along the 1200 km long, N-S trending, intra-arc LOFS (Cembrano *et al*. 1996). Transpressional recent tectonics cause dextral strike-slip movement on that fault zone. In the study area the LOFS runs along the N-S oriented Lake Caburgua and continues to the south in the Valley Palguin (between Villarrica Volcano and Quetrupillán Volcano). Near Liquiñe (southern margin of research area) a maximum width of 2 km is documented for the LOFS (Hervé 1976).

Additionally, NW–WNW and NE aligned fault zones are observed in the study area. The latter are considered as tension fractures related to the oblique maximum stress direction. NE trending fault zones occur in the investigation area on the NE flank of Villarrica Volcano (Cembrano & Lara 2009). NW aligned fault zones are common in the south Andean Cordillera (Bohm *et al*. 2002; Melnick *et al*. 2006). Oriented parallel to minimal horizontal stress, they undergo active compression.

In the vicinity of Villarrica Volcano, the ESE–WNW-aligned Mocha-Villarrica fault zone (MVFZ; Rapela & Pankhurst 1992; Hackney *et al*. 2006; Zaffarana *et al*. 2010) crosscuts and offsets the LOFS (Fig. 1). The fault zone is accompanied by the lineament of the volcanic chain Villarrica-Quetrupillán-Lanín. It offsets the LOFS by a few km to the west indicating sinistral movement (Lange *et al*. 2008).

The volcanic rocks from Villarrica-Quetrupillán-Lanín stratovolcanoes show a variable basaltic-dacitic (sometimes rhyolitic) geochemical composition (Moreno *et al*. 1994; Lara 2004) whereas minor eruptive centres, located to the north near the Caburgua lake and the Valley Liucura (Fig. 2), show a less fractionated, mainly basaltic, composition. From isotopic studies magma chambers below the stratovolcanoes are assumed in shallow depth (Hickey-Vargas *et al*. 1989), neglecting in contrast the presence of major chambers below the small eruptive centres. Unlike Quetrupillán and Lanín, Villarrica Volcano reveals a strong recent mostly Strombolian activity of basaltic-andesitic composition (Ortiz 2003; Hickey-Vargas *et al*. 2014).

These Holocene volcanic rocks overlie granitic and volcano-sedimentary formations (Fig. 1). The granitoids belong to the North Patagonian Batholith (Hervé 1984; Munizaga *et al*. 1988). This plutonic belt was emplaced between 39°-47°S during two phases in Late Cretaceous and Miocene times mainly along the trace of LOFS (Pankhurst *et al*. 1999). North of the volcanic chain the batholith is slowly replaced by Eocene-Miocene volcano-sedimentary units known as the Cura-Mallín formation (Jordan *et al*. 2001). In this time period extensional tectonics caused the formation of a sequence of sub-basins in south central Chile between 33°–39°S. Sedimentary thickness of up to 3000 km is documented (Radic 2010), filled with non-marine sediments intercalated with pyroclastic rocks and lava flows mainly of andesitic composition (Niemeyer & Muñoz 1983; Suarez & Emparan 1995).

3 DATA ACQUISITION

MT data were acquired mainly along two approximately E–W (25 km) and N–S (45 km) oriented profiles at the southern shore of Caburgua Lake and W of Villarrica volcano, respectively, including 31 MT stations (Fig. 2). These measurements were conducted between November and December 2013. Due to insufficient connection of the electrodes to the massive rock at seven stations on the western flank of the volcano, only the magnetic field was measured in March 2014. The orientation of the E-W MT profile was selected assuming that the major tectonic elements, the N–S striking LOFS and Andean subduction zone determine the geoelectric strike direction (Muñoz *et al*. 1990; Brasse & Soyer 2001). However, given the shallow target depth including major secondary fault orientations and considering the complex analysis of geoelectric strike by

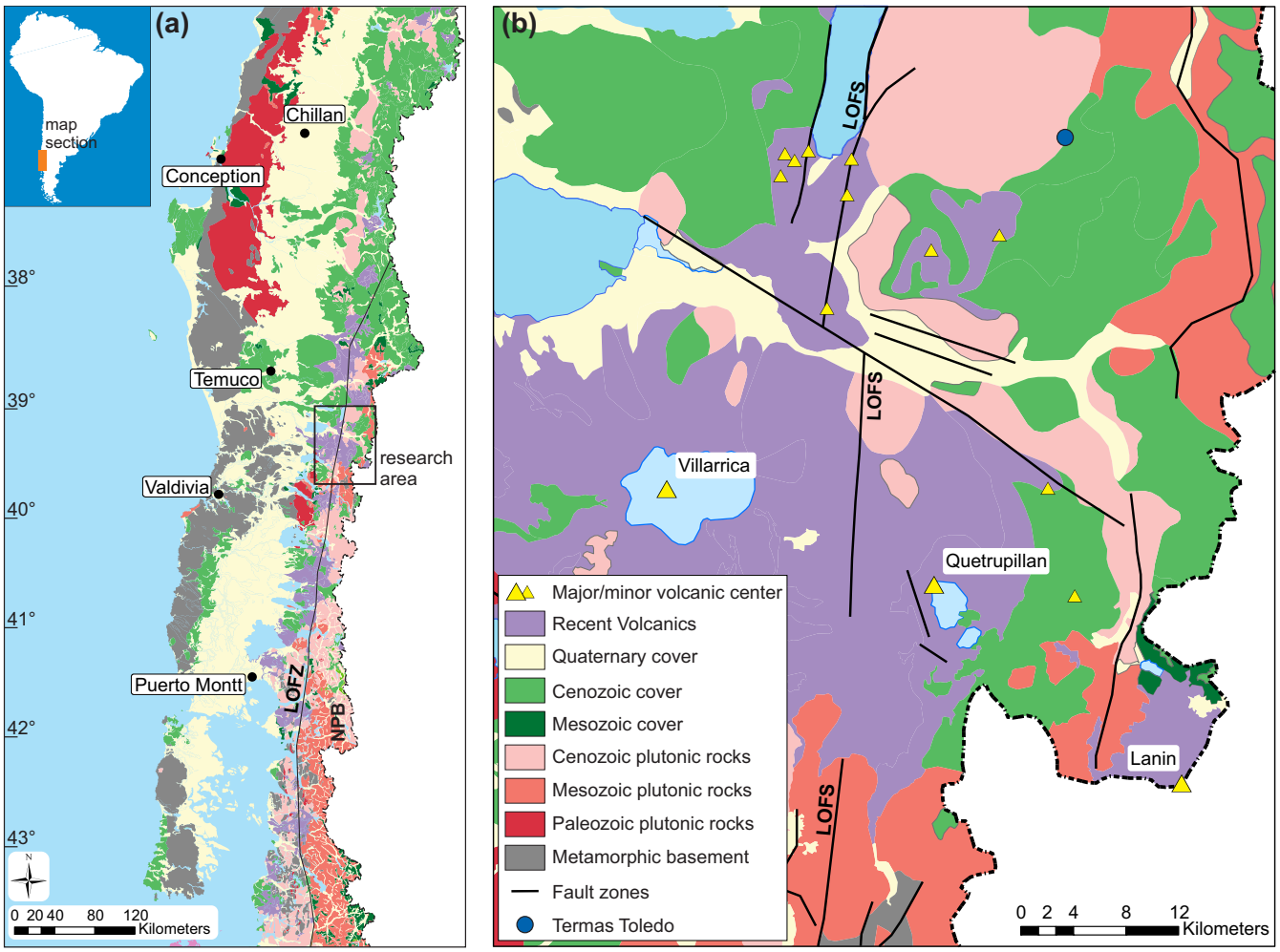

Figure 1. (a) Geological map of southern Chile across the Cretaceous-Mesozoic North Patagonian Batholith (NPB) at the southern rim of the study area to Meso-Cenozoic volcano-sedimentary basin fillings and the dextral intra-arc Liquiñe Ofqui Fault System (LOFS) crosscutting the NPB and continuing to the N in the sedimentary sequence. (b) Geological and structural map of the study area. Both modified after 1:1 000 000 scale map, Servicio Nacional de Geología y Minería, Chile by including interpretations from Moreno & Lara (2008), Cembrano & Lara (2009), Sánchez *et al*. (2013) and Lara & Moreno (2004).

Brasse & Soyer (2001), we must also consider a potentially deviating geoelectric strike. Therefore, a second profile has been chosen sub-perpendicular to the lineament of the volcanic chain Villarrica-Quetrupillán-Lanín and MVFZ. Although both structures strike approximately N120°E, the natural relief implied a 30° angle to the lot, that is, an N–S orientation of the profile.

In order to obtain high resolution at comparably shallow depth, that is, in the first kilometres of the crust, and to connect to its deeper parts (see Brasse *et al*. 2009), a period band of 10^{-3} to 512 s was chosen for data acquisition. The E–W profile was measured with an average spacing of 1–2 km in the central parts and up to 6 km in the outer part, while the N–S profile spans a total of 45 km with an average station distance of 2 km. A remote station was operated quasi-continuously for 26 d, with an interruption of 4 d due to animal activity, during the entire MT campaign. The station is situated at the eastern rim of the E–W profile (station 0 in Fig. 2).

Data were acquired over 1–3 d allowing for robust data processing. Measurements were carried out using four MT stations with an ADU-07e data logger, three MSF-07e coil magnetometers and four EFP-06 electrodes (Metronix Inc.). Magnetometers and electrodes were oriented N–S, E–W and vertical. All horizontal magnetic and electric sensors were buried at about 20 cm depth. The vertical magnetic sensor was buried completely. Cables were fixed to the surface and partly buried to reduce the influence of motion (e.g. by wind).

4 DATA PROCESSING AND RESULTS

Time series data were processed to determine the impedance tensor using mutual remote reference processing in order to reduce local electromagnetic noise (Gamble *et al*. 1979). The improvements of different processing steps and further optimization are shown for a representative example (site 5) in Fig. 3. Two different processing codes were applied: The WinGLink© code (Schlumberger, version 2.21) including a 50 Hz and harmonics notch filter yields high quality transfer function data at short periods ($T < 1$ s), but shows low-quality processing results at $T > 1$ s with out-of-quadrant phase data at all stations (e.g. Figs 3a–c). Therefore, at $T > 1$ s robust data processing techniques after Egbert & Booker (1986) were applied. The application of the notch filter improves data quality at higher frequencies significantly (e.g. Fig. 3b). Mutual remote

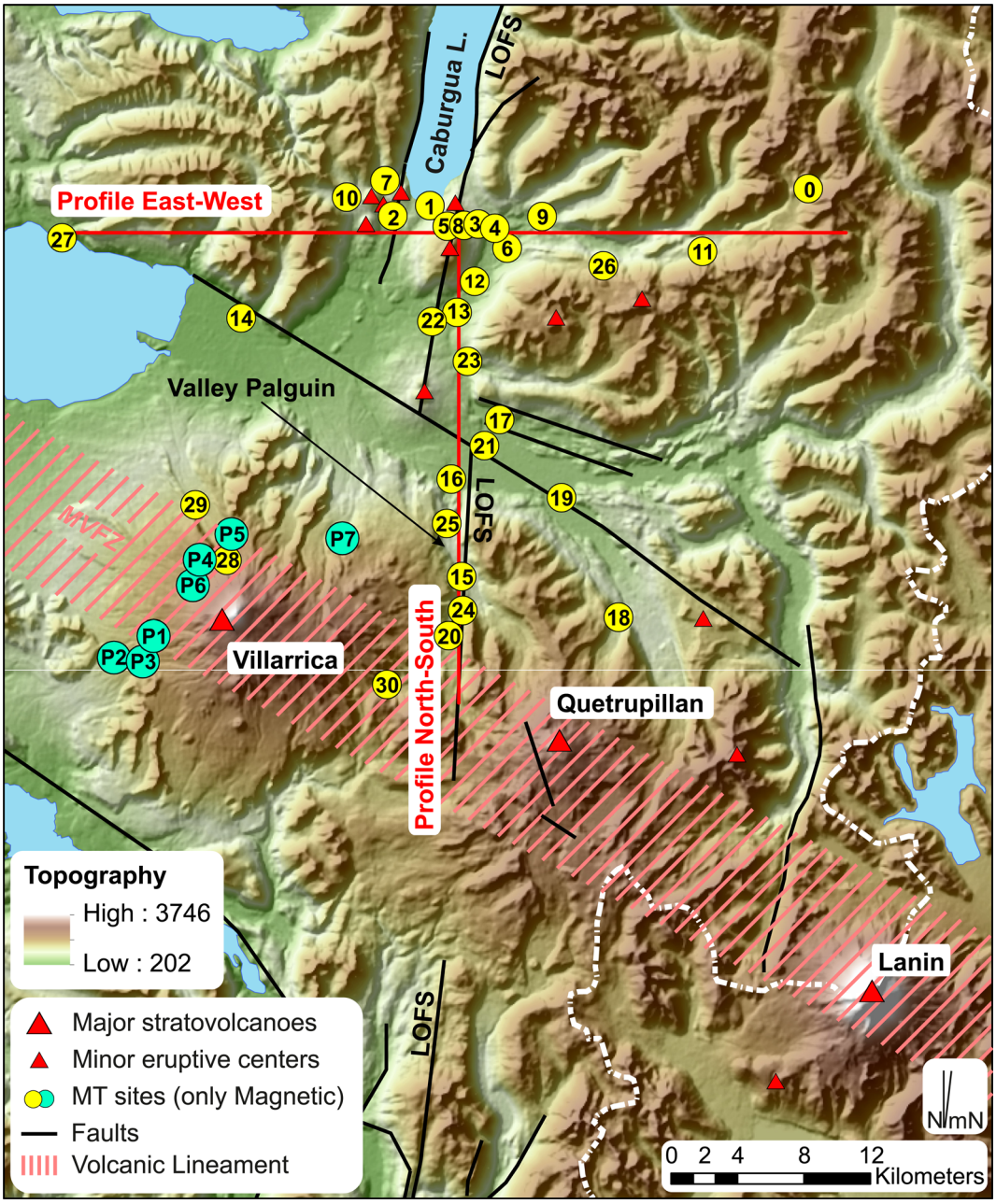

Figure 2. Shaded relief topographic map of the study area next to the Villarrica Volcano. Topography is based on SRTM data from NASA. Local fault zones according to Lara & Moreno (2004), Moreno & Lara (2008) and Sánchez *et al*. (2013). Numbered yellow dots: MT stations; numbered cyan dots: magnetic field stations; Station 0 represents the remote reference station; LOFS: Liquiñe Ofqui Fault System; N and mN: direction of geographic and magnetic north with a declination of 6.5°.

referencing technique enhance data quality mainly at intermediate periods $T = 0.1$–10 s (Fig. 3c). Acceptable quality of the transfer function is reached after merging the differently processed two period ranges, $T < 1$ s and $T > 1$ s (Fig. 3d).

Off-diagonal components of transfer functions Z of all MT stations are presented in the supplementary material. Note that although for six stations (12–17) remote processing is not applicable, rather smooth transfer function with equally small errors compared to remote processed sites are obtained in most cases.

Data quality has been assessed using the following criteria. Poor data quality is characterized by a change of apparent resistivity or phase between two periods by >1 order of magnitude or >15°. For inversion, individual data points were discarded, if of poor quality or if error bars exceed one order of magnitude (apparent resistivity) or more than 20° (phase angle). Finally, <10 per cent of individual outliers were excluded from inversion (transparent in Supplementary Material). Only station 22 was excluded completely from inversion.

4.1 Directionality and dimensionality analysis

In order to verify the validity of the initial assumption of 2-D distribution of subsurface structures as well as the potential geoelectric strikes, dimensionality and directionality have to be investigated. Generally, Swift skew values <0.1 (Swift 1967) allow for 1- or

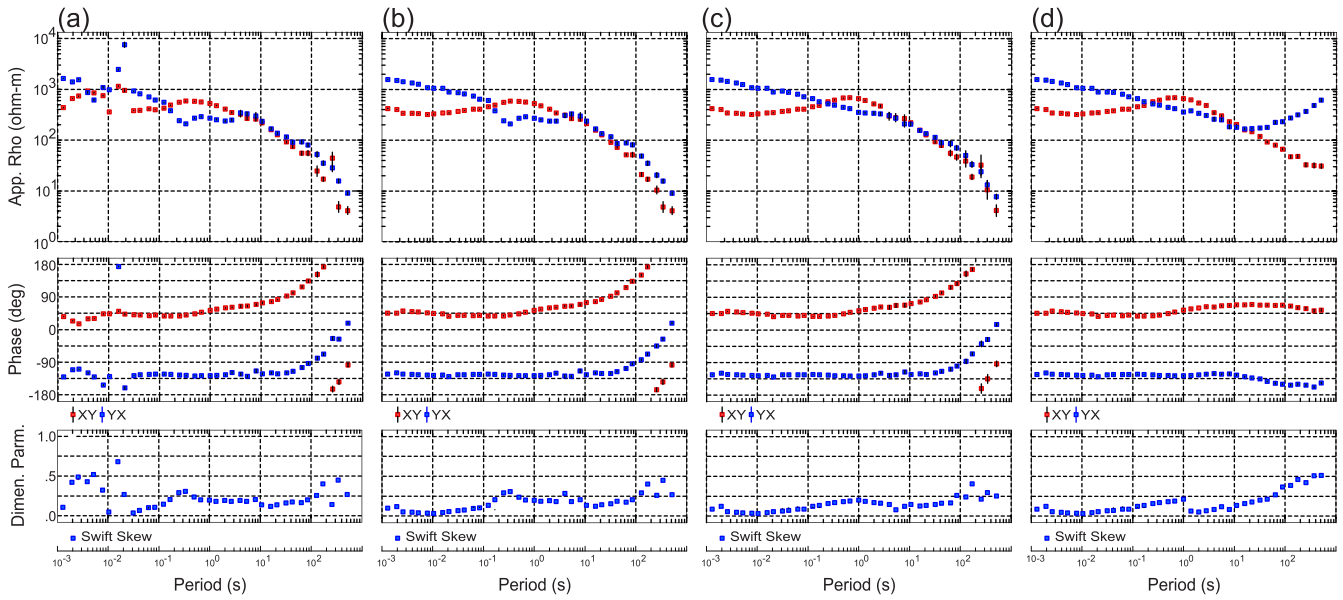

Figure 3. Representative transfer functions (site 5, Fig. 2) with successively enhanced processing steps from (a) single site processing, (b) single site processing including a 50 Hz and harmonics notch filter to (c) and (d) mutual remote reference techniques combined with notch filtering. Processing was carried out using WinGLink© software (Schlumberger, version 2.21) for all frequency ranges except in (d), when frequencies >1 s where processed using the Egbert & Booker (1986) algorithm due to out-of-quadrant behavior of the phase in (a)–(c).

2-D interpretation of the geoelectric structure of the subsurface for $T < 1$ s (Supplementary Material), but do not exclude 3-D conductivity distribution. Increasing Skew values at longer periods and particular stations with higher values at distinct frequencies suggest significant 3-D behaviour (Supplementary Material).

Neglecting galvanic distortion using impedance tensor decomposition after Bahr (1991) (eq. 1),

$$\eta = \frac{\sqrt{\left|\left[Z_{xx} - Z_{yy}, Z_{xy} + Z_{yx}\right] - \left[Z_{xx} + Z_{yy}\,, Z_{xy} - Z_{yx}\right]\right|}}{\left|Z_{xy} - Z_{yx}\right|} \quad (1)$$

hereafter called Bahr skew, most of the sites show values $\eta < 0.3$ for $T < 8$ s allowing for both, 2-D and 3-D interpretation (Fig. 4). At larger periods $T > 20$ s these low η-values are also prevailing. For $8\text{ s} \leq T \leq 20$ s, values are significantly higher indicating dominant 3-D resistivity distribution. Note that high Bahr skew values coincide with large errors in the transfer functions at higher periods (e.g. stations 3, 7 and 13 at $T \geq 8$ s, Supplementary Material). To address the geoelectric strike direction, a decomposition analysis was carried out after Becken & Burkhardt (2004) analysing the ellipticity of electric and magnetic field polarization (Fig. 5). Strike direction was determined using single-site, multi-frequency analysis for each MT station individually. Reduction of cumulative minimum ellipticity was achieved by splitting the total period range into three intervals (Fig. 5). Although high variation of strike direction is observed for $T < 0.1$ s, a principal strike direction of approximately N350°E to N7.5°E occurs at eleven of 31 stations. A secondary direction of approximately N120°E is observed at five sites. The latter is found to be the dominant direction in the period band $T = 0.1$–10 s occurring at eleven of 31 stations, whereas the roughly N–S direction is found at four sites, only. For $T > 10$ s, scattering is reduced and the dominant direction is found to be approximately N–S again.

It can be summarized that both assumptions, the 2-D distribution of structures in the subsurface and the two geoelectric strike directions, approximate natural subsurface conditions to a large extent.

4.2 Vertical magnetic field data

Induction arrows representing the real part of the magnetic field component are presented for different frequencies in Fig. 6 using Wiese convention (Wiese 1962), that is, induction arrows point away from relatively high conductive features. In agreement with skew analysis, for $T < 0.02$ s, they show strong scattering in direction and intensity (representative results at $T = 1/128$ s in Fig. 6). For $0.02\text{ s} < T < 0.5$ s ($T = 0.125$ s in Fig. 6), induction arrows east of the LOFS point towards E, whereas stations west of the fault point towards W. Supported by a small vertical magnetic field component at the fault zone (station 8 and 30), the presence of a conductor coinciding with the LOFS is indicated.

Stations located at the western flank of the volcano deviate from this pattern as they point away from the centre of the volcano. Although topographic effects cannot be ruled out completely, the arrow pattern does not display the topography of the Villarrica Volcano. With increasing distance to the Villarrica-Quetrupillán-Lanín lineament, the vertical magnetic component increases and is oriented perpendicular to this lineament. Thus, a conductor parallel to the lineament can be assumed. In contrast, at $T = 0.5$–6 s ($T = 1.39$ s in Fig. 6) the possible dominance of the LOFS on inductions arrows decreases, as they experience a general northeastward rotation and a reduction in intensity E of the LOFS. Induction arrows at stations possibly linked to the Villarrica-Quetrupillán-Lanín lineament remain unchanged with respect to smaller periods. Moreover more stations, also in greater distance to volcanic lineament, possess NE direction perpendicular to the volcanic chain.

At increasing depths ($T = 10$–50 s), induction arrows show a smaller vertical magnetic field component, indicating a homogenous electromagnetic interval ($T = 11.1$ s in Fig. 6). With increasing depth

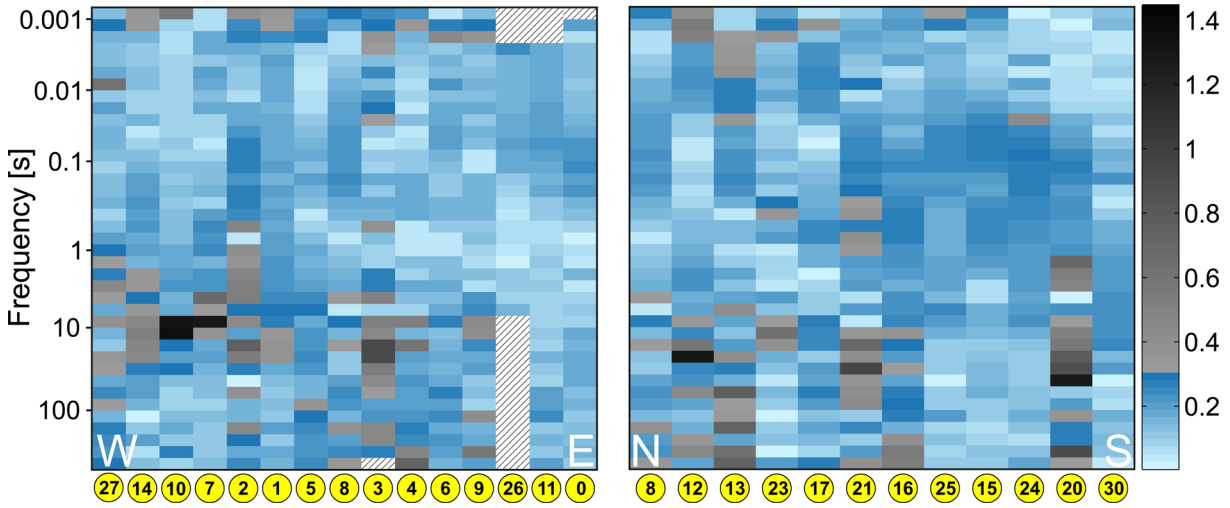

Figure 4. Evaluation of dimensionality using phase sensitive skew of impedance tensor after Bahr (1991) on the E–W profile (left) and N–S profile (right). Impedance tensors with skew values below 0.3 (indicated by blue colours) are valid for 2-D interpretation. Hatched areas: no data available.

the induction vectors rotate to NNW–NNE directions ($T = 512$ s in Fig. 6) described by Brasse *et al.* (2009) and interpreted as an anisotropy caused by a tensile fracture regime parallel to maximum horizontal stress.

4.3 Phase tensor

Phase tensor analysis after Caldwell *et al.* (2004) is used to determine the directional behaviour of the regional conductivity structures in the study area. The galvanic distortion independent phase tensor Φ can be written as

$$\begin{bmatrix} \phi_{11} & \phi_{12} \\ \phi_{21} & \phi_{22} \end{bmatrix} = \frac{1}{\det(X)} \begin{bmatrix} X_{22}Y_{11} - X_{12}Y_{21} & X_{22}Y_{12} - X_{12}Y_{22} \\ X_{11}Y_{21} - X_{21}Y_{11} & X_{11}Y_{22} - X_{21}Y_{12} \end{bmatrix} \quad (2)$$

with X and Y being real and imaginary part of the impedance tensor. The phase tensor can be visualized by an ellipse with the principle axes φ_{Max}, φ_{Min} representing the eigenvectors of the tensor. In this analysis, the angle α-β of φ_{Max} to the observer's coordinate system indicates preferred flow direction of regional induction currents. The phase tensor skew angle β completes the full description of the tensor. It is a measure of asymmetry in the regional MT response. While, comparable to Bahr and Swift skew, low values of the phase tensor skew are inconclusive, persistent directions of principal axes of the phase tensor with period and location along strike seem to provide good indication for approximation of 2-D subsurface conditions. φ_{Max} indicates conductivity gradients, in a 2-D case parallel or perpendicular to the regional geoelectric strike (Caldwell *et al.* 2004).

Fig. 7 displays the phase tensors at different periods. Although β values are significantly different from zero, indication for 2-D behaviour is indicated by rather consistent orientation of φ_{Max}. In general, a comparably high φ_{Max}: φ_{Min} ratio is observed for $T > 20$ s coinciding with a rather consistent orientation of φ_{Max} in N–S direction across the study area (Fig. 7d). Although absolute values of φ_{Max} and φ_{Min} increase in the interval $0.05 < T < 20$ s, a comparably low φ_{Max}: φ_{Min} ratio and a preferential φ_{Max} orientation of approximately N30°E is persistent throughout this period range (representative results at $T = 0.125$ s and 1.39 s in Figs 7b and c). At smallest periods, comparably low φ_{Max} and φ_{Min} are observed along with high directional scattering. In summary, the phase tensor analyses are consistent with observations from induction arrows and dimensionality analyses. All three allow for relating geoelectric data to tectonic structures in the study area.

5 INVERSION OF MT AND VERTICAL MAGNETIC FIELD DATA

Since dimensionality analyses do not exclude a 2-D subsurface structure to a large extend, but a change from N–S to N120°E in geoelectric strike is observed at intermediate periods, 2-D inversion was carried out on the two profiles (E–W and N–S in Fig. 2). Respecting the geoelectric strike, the measurements acquired at stations along the N–S profile have been rotated by 120°. Inversion of MT data was carried out employing TE, TM modes and the vertical magnetic field transfer function individually or in different combinations on rectangular meshes with a size of 1075 × 480 km and 165 × 100 cells for the E–W profile and 1058 × 480 km and 140 × 90 cells on the N–S profile including topography. The 2-D nonlinear conjugate gradients algorithm (Rodi & Mackie 2001) minimizes the misfit between modelled and observed data with a regularization term related to the spatial smoothness of the modelled resistivity distribution. Smoothing parameter τ describes the ratio between roughness and data misfit. The trade-off between data fit and model smoothness is analysed in Fig. 8 after Hansen & O'Leary (1993). Using a reduced mesh size of 65 horizontal × 36 vertical elements inversion results are obtained for $\tau = 0.3$ to $\tau = 300$. Based on the L-curve smoothing parameters $\tau = 7.5$ was selected for further inversion. It should be noted that main features are persistent through the variations of τ hinting on robust features (Fig. 8).

Since our inversion concept is based on 2-D subsurface structures for distinct depth ranges and TE modus is more sensitive to 3-D effects, a parameter set A with a higher error floor of 70 per cent for TE apparent resistivity compared to 15 per cent for TM mode after Becken *et al.* (2008) is applied. Compared to phase error floor of 5 per cent, the error floors of apparent resistivity are higher to reduce static shift. For the vertical field data an absolute error floor of 0.065 was used. Since we aim at linking near-surface structures to deep MT soundings, a second set of inversion parameters approximating Brasse *et al.* (2009) has been used. This dataset B weights TE and

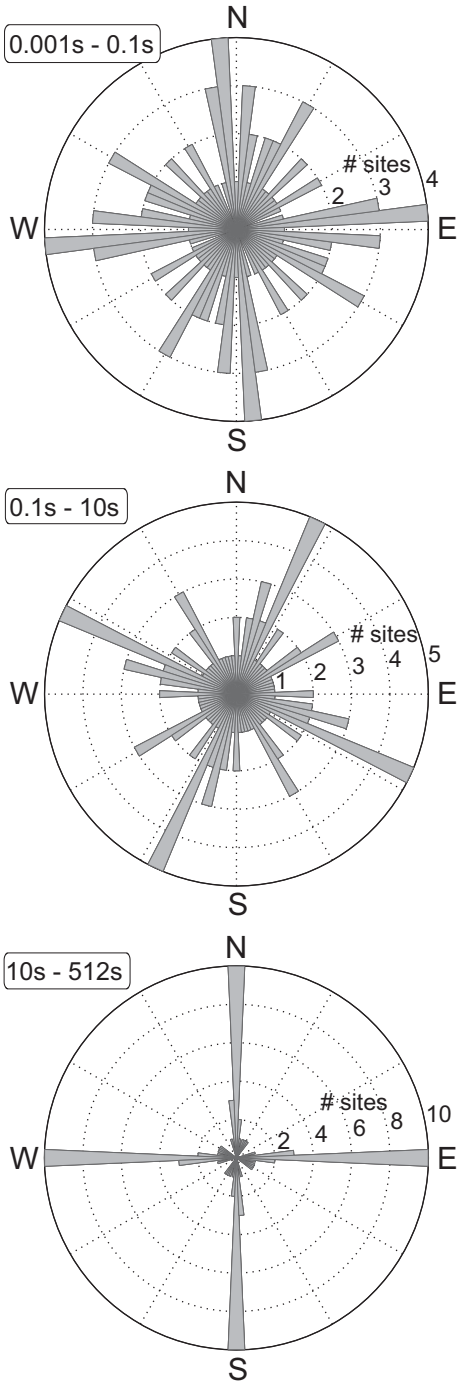

Figure 5. Directionality analysis after Becken & Burkhardt (2004) using regional strike mode determining a single strike at each station. With exception of the period range of 10–512 s, for which data availability and quality reduces the stations to 21, all 31 stations were analysed. Results were divided in period ranges manually yielding intervals of different prevailing strike regimes.

TM modes equally analysing effects of 3-D resistivity distribution with error floors of 20 per cent for apparent resistivity, 5 per cent for phases and 0.1 for vertical field data. To constrain the electromagnetic features manual sensitivity tests were performed by fixing resistivities to replace conductive/resistive features and the omission of single sites. All features discussed in the following show robust behaviour.

Inversions were started from 100 Ωm uniform half space. Additional test inversions starting from a 500 Ωm uniform half space yield similar results. Inversion results after 150 iterations with an average RMS misfit of 1.86 (set A) and 2.14 (set B) for the E–W and 2.14 (set A) and 2.32 (set B) for the N–S profiles, respectively, are shown in Fig. 9(a). Note that errors of set B exceed errors of set A significantly near the deep conductor (Con2). Inversion results are presented for inversion parameter sets A (Fig. 9b) and B (Fig. 9c) for both profiles, E–W and N–S to a depth of 32.65 and 26.00 km, respectively. From 2-D inversion of the two profiles four major features can be identified:

(1) In the E–W profile, E of station 27, a high resistivity layer with ρ up to >5000 Ωm is observed at near-surface to a depth of about 7.5 to 12 km. Such a high resistive layer can also be observed in the central part of the N–S profile below stations 13 to 25. Station 27 is located at the transition from the volcanic chain to the longitudinal valley to the W, which is filled with up with 5 km thick sediments.

(2) In the E–W profile, a narrow rather vertical structure of moderate conductivity (Con1) with $\rho = 100$ Ωm intersects this high resistivity structure below stations 5 and 8 to a depth of approximately 10 km. This anomaly continues about 5 km to the S as shown in the N–S profile underneath stations 08 and 12. Using parameter set B, in the N–S profile it appears more conductive. We consider this to be a boundary effect. Tests using fixed resistivity inversion exclude Lake Caburgua as a possible origin of this anomaly.

(3) At a depth of about 20 km, a deep conductor Con2 with ρ up to 10 Ωm appears at the eastern part of the E–W profile in inversion parameter set A extending to the lower boundary of the section. In parameter set B, this Con2 is characterized by a resistivity of up to ∼30 Ωm and a slight offset to the W. Corresponding RMS is significantly higher compared to parameter set A. These resistivities and the lateral location are consistent with the anomaly C in Brasse & Soyer (2001) and B in Kapinos *et al*. (2016).

(4) Along the N–S profile, a second moderate conductor (Con3) with $\rho \geq 20$ Ωm is indicated in the southern part below stations 24 and 20. Con3 seems to be part of a larger structure with an apparent northward dip. It is located below the volcanic lineament.

Since this study aims at a possible connection of mid-crustal conductors to major fault zones, we first investigate the origin of Con1 coinciding with the LOFS near Lake Caburgua using simple forward modelling of end member scenarios (Fig. 10). Two scenarios have been tested based on geological and resistivity observations. Scenario 1 (Fig. 10a) assumes the width of LOFS bound by the faults E and W of Lake Carburgua (Fig. 2) resulting in a width of 2 km. Scenario 2 (Fig. 10b) starts from a width of 0.25 km based on Con1 at near-surface (see station 8 in Fig. 9). Following minimum resistivity of Con1 gained from inversion, for the forward modelling the start value was set to 100 Ωm for scenario 1 and 30 Ωm for scenario 2. Synthetic MT data were generated by forward modelling adding a 5 per cent Gaussian noise. Parameter set A was used for the inversion, which was terminated after 150 iterations allowing for a comparison between synthetic and measured data. Both scenarios trace equally well the high resistivity contrast from up to >5000 Ωm to about 100–200 Ωm at about 10 km depth and are able to reproduce Con1. The shape of the Con1 is well traced by forward modelling results of scenario 2, whereas the width of Con1 at a depth of about 5 km seems to be related to a broader structure such as assumed in scenario 1. We would like to point out here that although not matching Con1 at near-surface, a combination of the two scenarios, that is, a so-called flower structure, possibly reproduces best Con1.

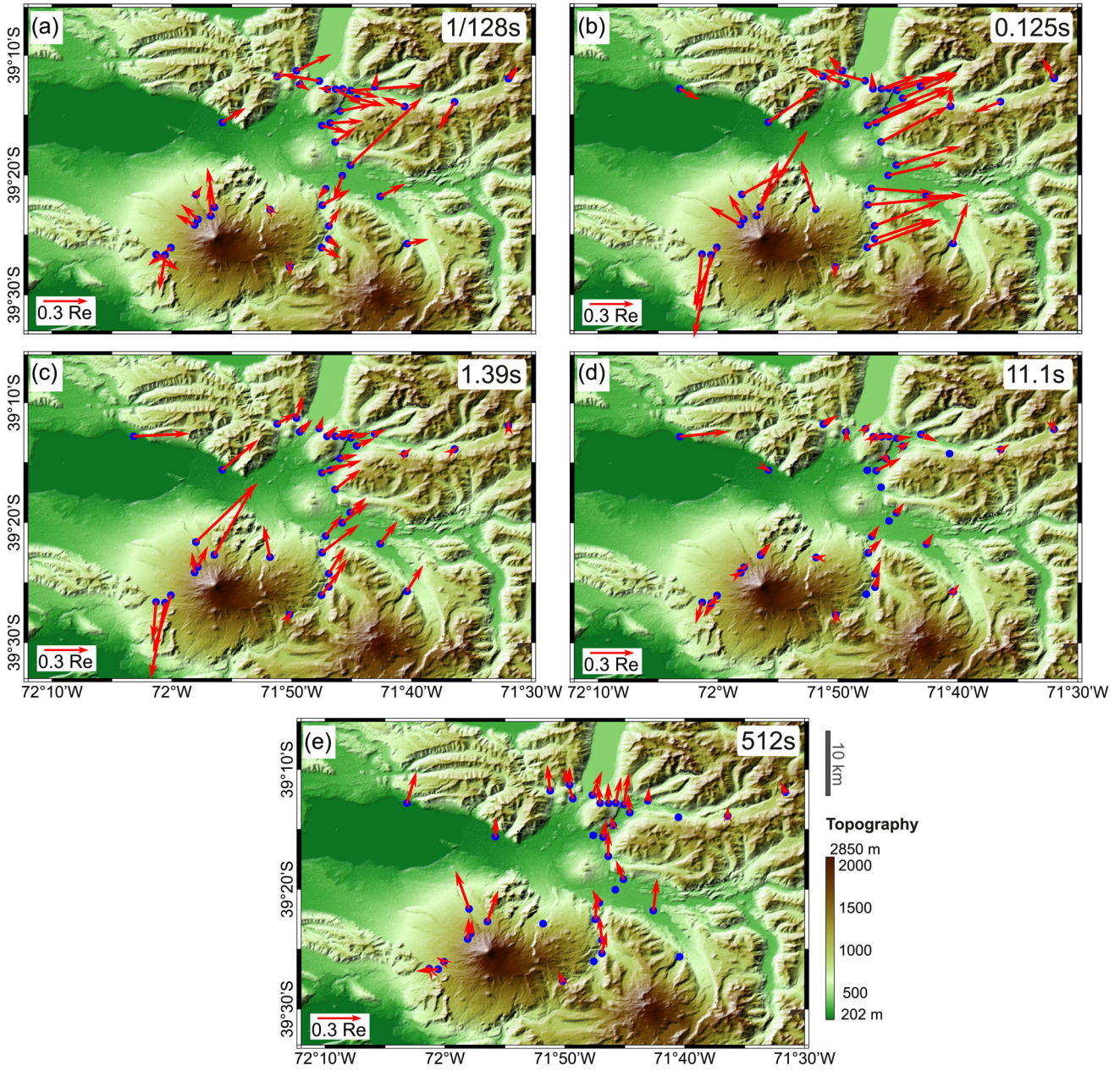

Figure 6. Induction arrows of representative frequencies (Wiese convention, Wiese 1962). Selected periods show effects of local, shallow fault zones (1/128 s, 0.125 s, 1.39 s), an electromagnetically homogenous depth interval (11 s) and a strong southward directed electromagnetic signal caused by an unknown conductor/mechanism first described by Brasse *et al*. (2009).

6 DISCUSSION

Generally, the results from MT measurements in the Villarrica area are subdivided in three depth sections that are characterized by differences in dimensionality, resistivity and directional behaviour. The three period ranges, near-surface (about 10^{-3} to 10^{-1} s), intermediate (about 10^{-1} to 10^{1} s) and long-period ranges, represent depth section of about <10 km, 10–20 km and >20 km, respectively. The near surface is characterized by N–S/E–W geoelectric strike directions prevailing over scattering. A link to the LOFS and thus an N–S preferential strike direction can be concluded from induction arrows. Coinciding with relatively low phase angles in the period range of $T < 5 \times 10^{-2}$ s, this period range is characterized by ρ up to >5000 Ωm, except from the LOFS, where moderate conductivity (Con1) with $\rho = 100$ Ωm intersects this high resistivity layer. The vertical transition to intermediate resistivity of about 100–200 Ωm occurs in a narrow depth range of about <2 km. The change from high to intermediate background resistivity points to the brittle-ductile transition. Bailey (1990) predicted a conductive lower crust, where fault zones are not able to penetrate into the ductile zone, as enhanced vertical permeability will empty the saturated lower crust rapidly reducing conductivity.

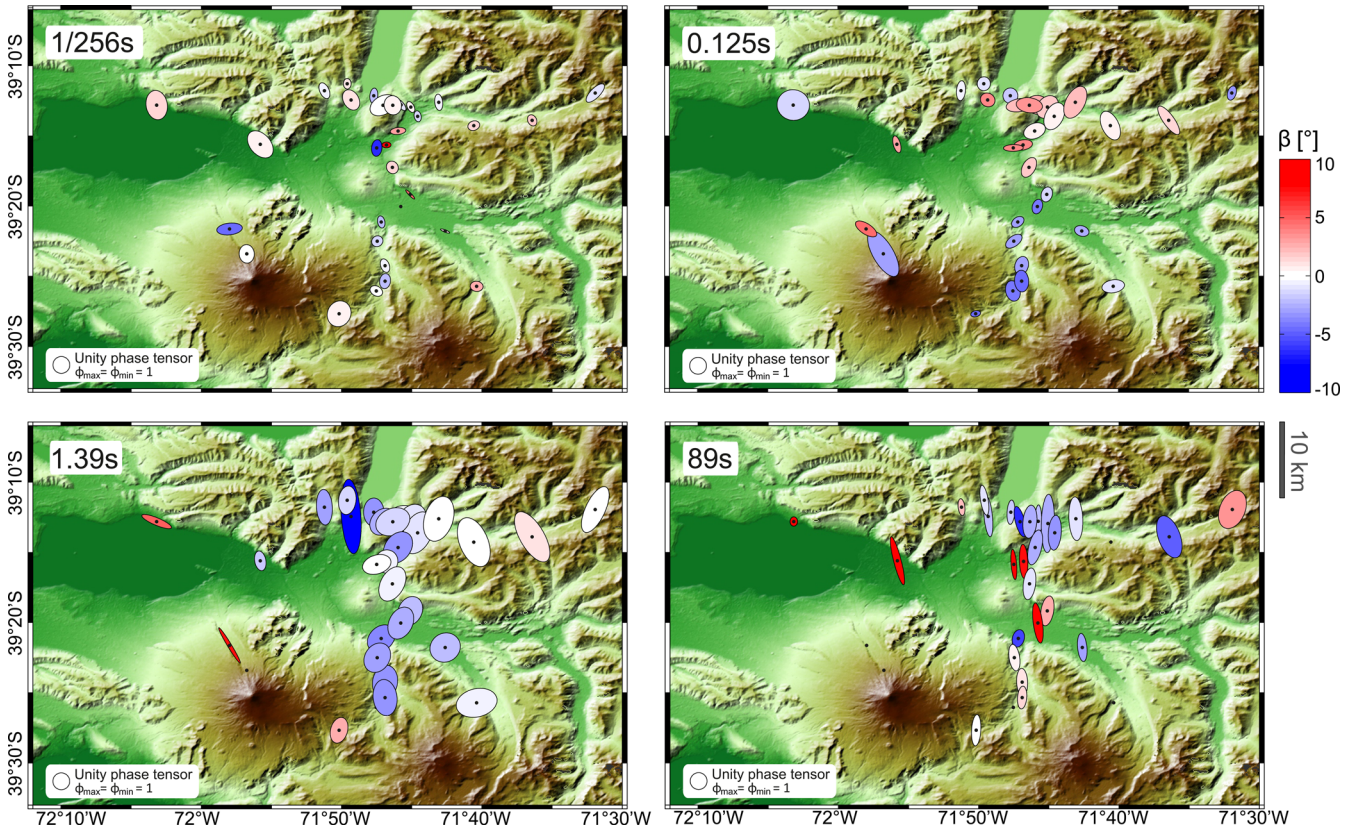

Figure 7. Phase tensor ellipses at different periods (after Caldwell *et al*. 2004). Lengths of the axes are proportional to principle values (φ_{max}, φ_{min}) of the phase tensor. Major axis rotated from E–W direction by angle α-β, (see description of α and β in the text). Colour code of ellipses display the skew angle β, describing the phase tensor asymmetry.

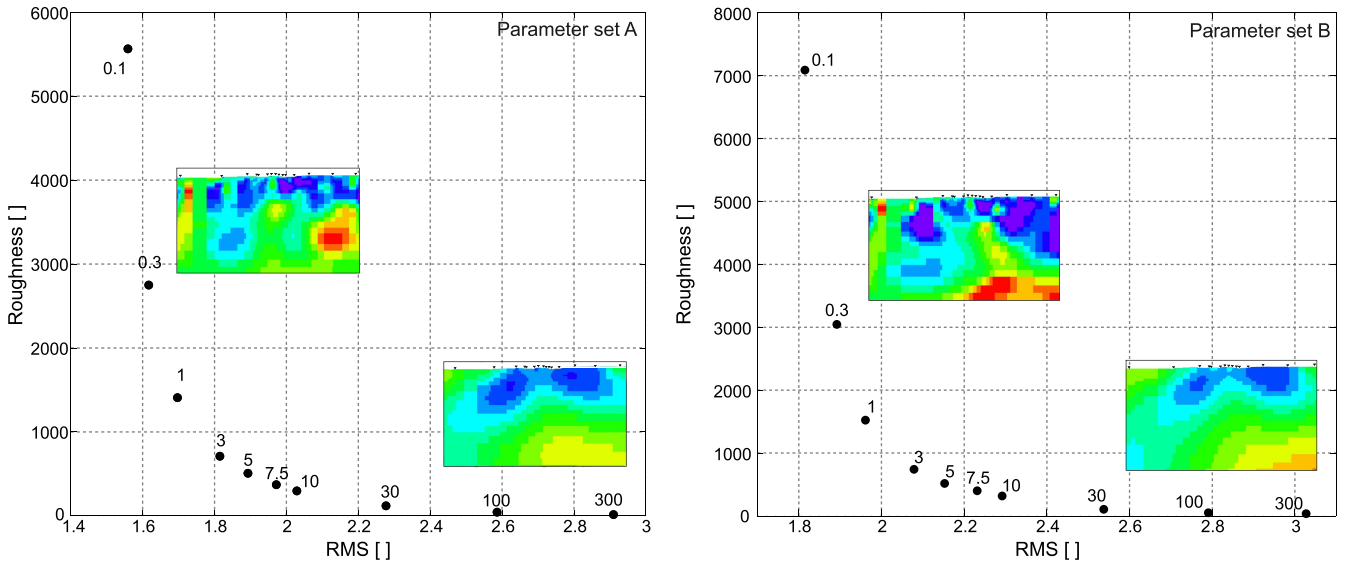

Figure 8. Model roughness versus root mean square (RMS) data misfit for smoothing parameter values τ between 0.3 and 300 for parameter set A (ρ(TE) = 70 per cent, ρ(TM) = 15 per cent, φ(TM, TE) = 5 per cent, Tx = 0.065) and B (ρ(TE) = 20 per cent, ρ(TM) = 20 per cent, φ(TM, TE) = 5 per cent, Tx = 0.1). Pictures presenting modelling results of the E–W profile smoothing parameters $\tau = 0.3$ and $\tau = 300$. Resistivity colour scale as in Fig. 9.

Ivanov & Ivanov (1994) observed this phenomenon for fault zones worldwide. Below, geoelectric strike direction changes in the intermediate section to ESE–WNW, indicated in both the directionality and induction arrow analyses. In agreement with the observation of Brasse *et al*. (2009), the geoelectric strike at long periods is clearly N–S/E–W oriented. At this depth, our results connect to the low resistivity anomalies observed during long-period MT measurements.

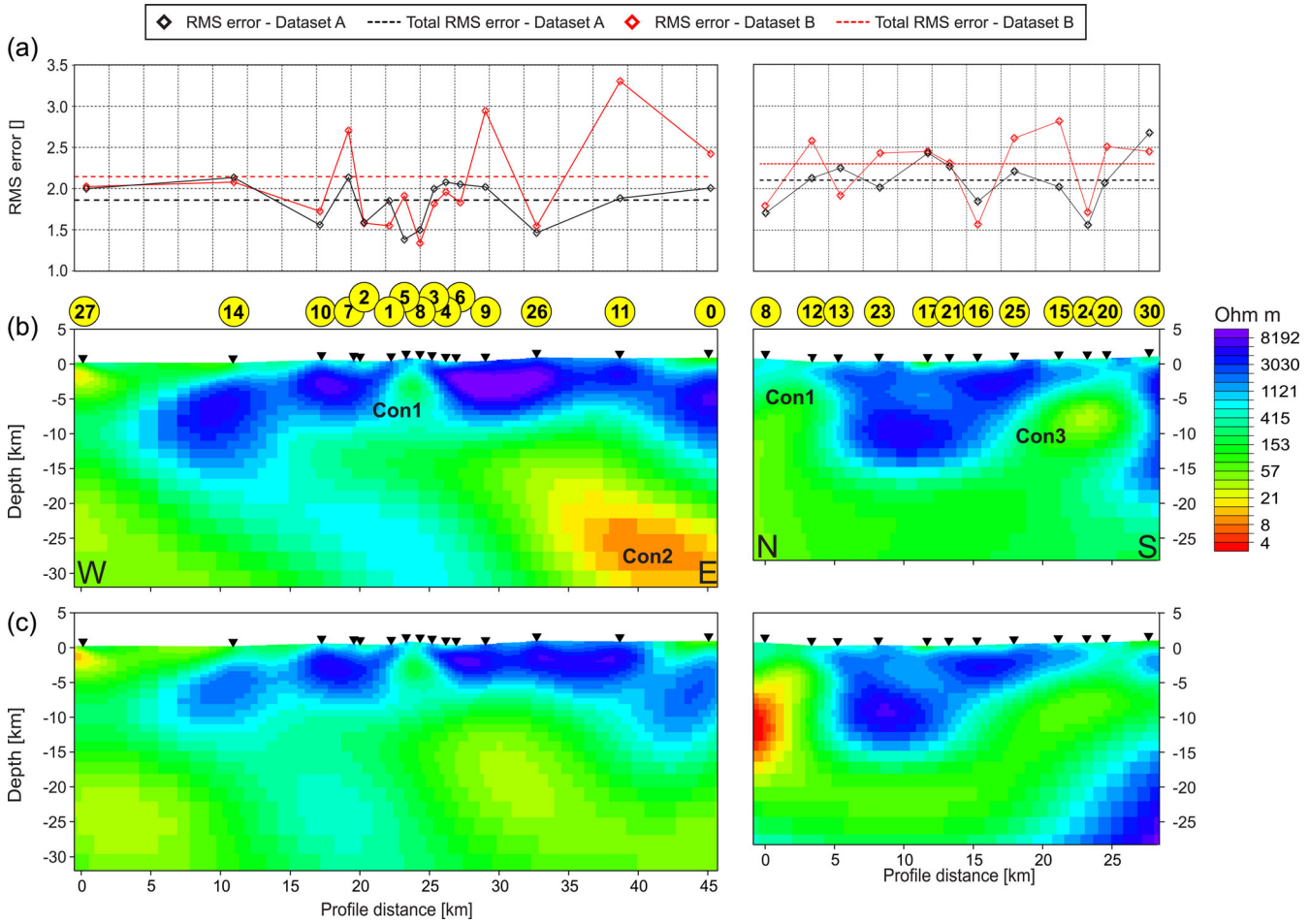

Figure 9. Inversion of MT data along the E–W (left) and N30°E profile (right) for parameter sets A (error floors 70 per cent for TE apparent resistivity, 15 per cent for TM apparent resistivity, 5 per cent for the phases, 0.065 for the vertical field) and B (error floors 20 per cent for apparent resistivity, 5 per cent for the phases, 0.1 for the vertical field). (a) Individual MT station RMS (dots) and average RMS across the profile (dashed lines) for parameter sets A and B after 150 iterations. (b) Results of inversion of MT data using parameter set A. (c) Results of inversion of MT data using parameter set B.

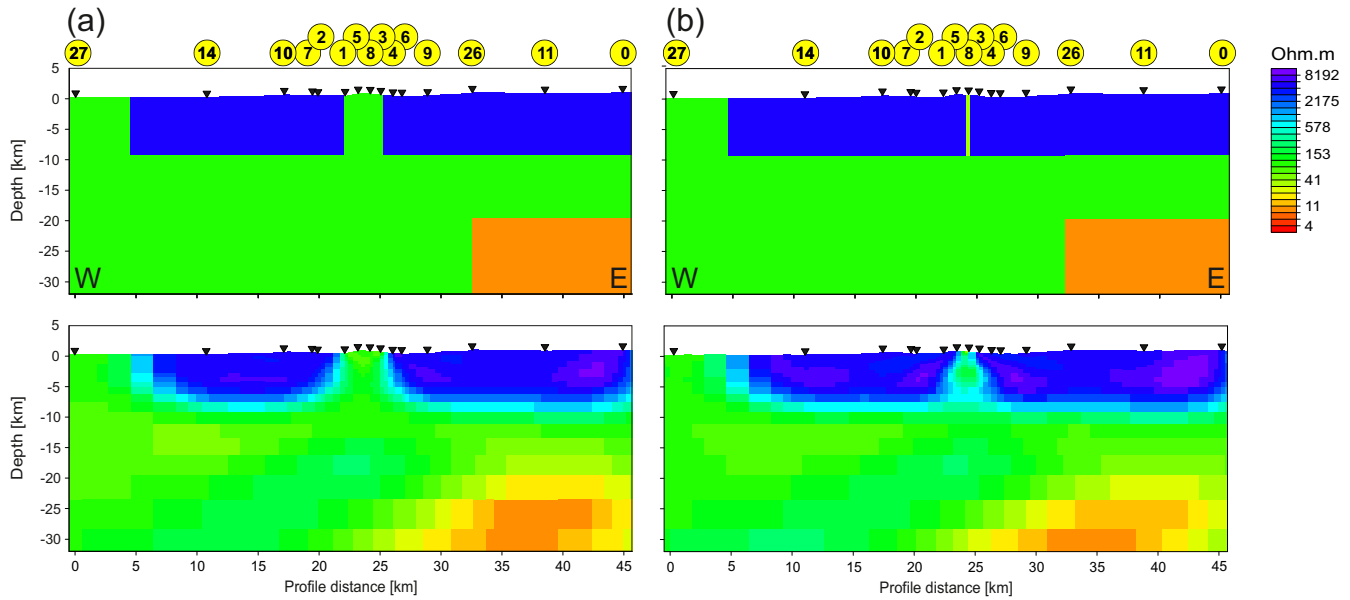

Figure 10. Forward modelling of end member scenarios for the width of LOFS (5 per cent Gaussian noise). (a) Following the width of the LOFS at Lake Caburgua (most likely representing a pull-apart structure), an upper limit of 2 km has been used for scenario 1. (b) Following the width of the low resistivity at the surface (Fig. 9), a lower limit of 0.25 km has been used for scenario 2.

In order to further characterize these high conducting structures their possible origin is discussed subsequently. The brittle-ductile transition is generally observed at a depth of 10–15 km coinciding with a temperature range of 250–500 °C (Sibson 1977; Ivanov & Ivanov 1994). Taking into account the local heat flow density of 130–170 mW m^{-2} (Hamza & Muñoz 1996), assuming an average thermal conductivity of 2.8 W m^{-1} K^{-1} and a radioactive heat production of 5 μW m^{-3}, we may estimate that the temperature at 10 km depth exceeds the critical temperature for the brittle-ductile transition. This hypothesis is supported by the coincidence of crustal conductance and a seismically quiet zone below 10 km depth, observed N of the study area (Bohm *et al*. 2002; Lange *et al*. 2008).

In summary, the intermediate resistivity anomalies Con1 and Con3 indicate fault controlled systems that can form a connection from mid-crustal depth (Con2) to near surface. Comparably high conductivity in faults zones has been attributed to clay alteration or saline fluids. In the following, bulk resistivity of about 30 Ωm of the fault zone related to Con1, obtained from forward modelling is investigated for clay content, porosity and cementation factor for fluid filled pores after Archie (1942) assuming that the tortuosity factor $a = 1$ (eq. 3) and for coupled fluid and clay filled pores after Waxman & Smits (1968) (eq. 4).

$$\sigma_B = \sigma_f \cdot \theta^m \tag{3}$$

$$\sigma_B = \theta^m \ (B \cdot Q_v + \sigma_f) \tag{4}$$

where σ_B and σ_f are the specific electric conductivities of saturated bulk rock and the fluid phase, θ the porosity, m the cementation factor, Q_v the concentration of sodium exchange cations in clay minerals and B represents an empirical equivalent conductance of the counterions as a function of σ_f. For determination of σ_f, 10 per cent dilution, indicated by chlorofluorocarbon analysis, has been considered to the maximum $\sigma_f = 1340$ μS cm^{-1} measured at Termas Toledo (Fig. 1). Conductivity correction to reservoir temperature has been carried out after Dakhnov (1959). Maximum reservoir temperature of 140 °C has been estimated from sulfate geothermometry for the low mineralized geothermal fluids in the study area (Held *et al*. 2015). Following eq. (3) with a generally accepted cementation factor of $m = 2$ for highly consolidated rocks, high values of about 26 per cent of fracture porosity are obtained (column 2 of Table 1). We may either assume that the cementation factor in the fault zone is reduced by mechanical damage or that the high conductivity is related to considerable clay content for which eq. (3) is not valid. For the latter calculations were performed using eq. (4) assuming that matrix resistivity exceeds by far the clay or fluid resistivity, and a cation exchange capacity (CEC) of non-swelling clay minerals CEC = 20 meq per 100 g. In eq. 4 CEC is incorporated in Q_v (see Waxman & Smits 1968). For both effects, we reduce the percentage of fracture porosity (Table 1).

Table 1. Calculations of required porosities assuming a plausible range of clay content (columns) and cementation factors (rows). n/a: determined resistivity (= 30 Ωm) cannot be achieved using this porosity/clay content composition.

	Archie 1942	Waxman & Smits 1968				
		% Clay				
m	0	1	5	10	15	25
1	6.9	4.1	n/a	n/a	n/a	n/a
1.5	16.9	15.2	9.3	4.5	2.3	0.9
2	26.3	25.1	21.1	16.7	13.3	9.1

The origin of enhanced conductivity at Con2 is assumed to be caused by partial melting. The melt fraction of Con2 can be roughly estimated after Glover *et al*. (2000) (eq. 5).

$$\sigma_B = \sigma_m(1 - \chi_m)^p + \sigma_f(1 - \chi_f)^m \tag{5}$$

where σ_B, σ_m and σ_f are the conductivities of bulk rock, melt fraction and fluid phase, χ_m the χ_f the volume fraction of melt and fluids and p and m the cementation factors of each phase. Cementation factor for melt is best represented by $m = 1.3$ (ten Grotenhuis *et al*. 2005). Electrical conductivity of molten rock was estimated to range between 1 and 30 S m^{-1} (Lebedev & Khitarov 1964; Tyburczy & Waff 1983). Bulk rock resistivity of <10 Ωm was achieved by adding 1.1 per cent melt with melt conductivity of 30 S m^{-1} or 2.7 per cent with melt conductivity of 10 S m^{-1}. Note that in the in the vicinity of stations 26 and 11 young volcanic edifices (Cerro Redondo and Relicura) are observed (Moreno & Lara 2008) supporting the hypothesis of partial melt generating Con2.

The penetration of a fault into the ductile zone may result in a listric fault geometry (e.g. Brun & Wenzel 1991). In the case of the Villarrica area, Con2 and other mid-crustal conductors coincide with deep rooted, regional fault zones (Kapinos *et al*. 2016). The inversion and end-member case forward modelling results of the broad-band MT data indicate that the connection between Con2 and the near surface Con1 is possibly masked by the decrease of the resistivity contrast below the brittle ductile transition.

Con3 reaches shallow subsurface level at the eastern flank of the Villarrica volcano. This part of the volcano revealed seismic activity at shallow depth during the last eruption in March 2015 (OVDAS 2015). With depth the Con3 structure shows an apparent northward dip down to about 20 km depth where it disappears in the general intermediate crustal conductive layer. Connecting the two profiles, even a dip towards NNE can be imagined for this anomaly. This would follow the directions of the major tectonic structures such as the volcanic chain lineament and the MVFZ. Induction arrows at intermediate to large depth support the occurrence of a conductive structure running parallel to the volcanic chain as well. This hints at a possible connection between Con2 and Con3.

7 CONCLUSIONS

High-resolution and broad-band MT measurements of the Villarrica Volcano area contribute to the understanding of the geothermal and tectonic setting of the area by indicating the geometry of the major structural elements. They provide additional support on the hypothesis of a connection between mid-crustal conductors and regional fault zones. The following observations are the most significant:

(1) Generally, high resistivities are observed in the upper 10–15 km followed by intermediate resistivities below. They are separated by a rather sharp contrast, which is likely to represent the brittle-ductile transition.

(2) In the upper crust the LOFS is characterized by a subvertical conductor (30 Ωm) down to a depth of about 10 km with enhanced conductivities, which may be attributed to partly interconnected, most likely fracture porosity and/or clay fillings.

(3) In the lower crust a high conductivity anomaly (5 Ωm) reveals a tendency to connect to near-surface anomalies. This is however probably masked by low resistivity contrast between LOFS and the ductile crust.

Our results show that mid-crustal conductors in southern Chile might be connected to major fault zones. In line with indication from 3-D inversion of long-period MT data, they are most likely connected to the WNW–ESE striking features such as the volcanic lineament or the MVFZ. The variability in geoelectric strike in the short to long period MT data suggests the application of full 3-D inversion, which will be published in a forthcoming paper. Further key questions concern the relation between the amount of fluid and type of deformation in strike-slip faults. The study area around Villarrica offers the exceptional opportunity to analyse the fluid composition of thermal springs and their relation to the regional tectonic features.

ACKNOWLEDGEMENTS

The study is part of a collaborative research project between Karlsruhe Institute of Technology (KIT) and the Andean Geothermal Center of Excellence (CEGA, Fondap-Conicyt 15090013). The authors appreciate the support from the BMBF-CONICYT International Scientific Collaborative Research Program (FKZ 01DN14033/ PCCI130025). Additional support from the Helmholtz portfolio project 'Geoenergy' in the topic 'Geothermal Energy Systems' and EnBW Energie Baden-Württemberg AG is gratefully acknowledged. Special thanks to the highly motivated team of students from University of Chile for the field measurements is expressed. We are grateful to Bernhard Friedrichs' (Metronix Inc) fruitful remarks during pre-processing, to Michael Becken's provision of his Matlab tool for the dimensionality analysis and to Adele Manzella and Cristina Pomposiello for their constructive review of the manuscript.

REFERENCES

Angermann, D., Klotz, J. & Reigber, C., 1999. Space-geodetic estimation of the Nazca-South America Euler vector, *Earth planet. Sci. Lett.,* **171,** 329–334.

Archie, G.E., 1942. The electrical resistivity log as an aid in determining some reservoir characteristics, *Trans. AIME,* **146,** 54–62.

Bahr, K., 1991. Geological noise in magnetotelluric data: a classification of distortion types, *Phys. Earth planet. Inter.,* **66**(1–2), 24–38.

Bailey, R.C., 1990. Trapping of aqueous fluids in the deep crust, *Geophys. Res. Lett.,* **17**(8), 1129–1132.

Barazangi, M. & Isacks, B.L., 1976. Spatial distribution of earthquakes and subduction of the Nazca plate beneath South America, *Geology,* **4,** 686–692.

Becken, M. & Burkhardt, H., 2004. An ellipticity criterion in magnetotelluric tensor analysis, *Geophys. J. Int.,* **159**(1), 69–82.

Becken, M., Ritter, O. & Burkhardt, H., 2008. Mode separation of magnetotelluric responses in three-dimensional environments, *Geophys. J. Int.,* **172,** 67–86.

Bedrosian, P.A., 2002. Magnetotelluric imaging of the creeping segment of the San Andreas Fault near Hollister, *Geophys. Res. Lett.,* **29**(11), 1–4.

Bohm, M., Lüth, S., Echtler, H., Asch, G., Bataille, K., Bruhn, C., Rietbrock, A. & Wigger, P., 2002. The Southern Andes between 36° and 40°S latitude: seismicity and average seismic velocities, *Tectonophysics,* **356**(4), 275–289.

Brasse, H. & Soyer, W., 2001. A magnetotelluric study in the Southern Chilean Andes, *Geophys. Res. Lett.,* **28**(19), 3757–3760.

Brasse, H., Kapinos, G., Li, Y., Mütschard, L., Soyer, W. & Eydam, D., 2009. Structural electrical anisotropy in the crust at the South-Central Chilean continental margin as inferred from geomagnetic transfer functions, *Phys. Earth planet. Inter.,* **173**(1–2), 7–16.

Brun, J.P. & Wenzel, F., 1991. Crustal-scale structure of the southern Rhinegraben from ECORS-DEKORP seismic reflection data, *Geology,* **19**(7), 758–762.

Caldwell, T.G., Bibby, H.M. & Brown, C., 2004. The magnetotelluric phase tensor, *Geophys. J. Int.,* **158**(2), 457–469.

Cembrano, J. & Lara, L.E., 2009. The link between volcanism and tectonics in the southern volcanic zone of the Chilean Andes: a review, *Tectonophysics,* **471,** 96–113.

Cembrano, J., Hervé, F. & Lavenu, A., 1996. The Liquifie Ofqui fault zone: a long-lived intra-arc fault system in southern Chile, *Tectonophysics,* **259,** 55–66.

Dakhnov, V.N., 1959. *Geophysical Well Logging,* Moscow Petroleum Institute, Q. Colorado Sch. Mines, Translated by G.V. Keller (1962).

Egbert, G. & Booker, J., 1986. Robust estimation of geomagnetic transfer functions, *Geophys. J. Int.,* **87,** 173–194.

Frost, B.R., Fyfe, W.S., Tazaki, K. & Chan, T., 1989. Grain boundary graphite in rocks and implications for high electrical conductivity, *Nature,* **340,** 134–136.

Gamble, T.D., Goubau, W.M. & Clarke, J., 1979. Magnetotellurics with a remote magnetic reference, *Geophysics,* **44**(1), 53–68.

Geiermann, J. & Schill, E., 2010. 2-D Magnetotellurics at the geothermal site at Soultz-sous-Forêts: resistivity distribution to about 3000 m depth, *C. R. Geosci.,* **342**(7–8), 587–599.

Glover, P.W.J., Hole, M.J. & Pous, J., 2000. A modified Archie's law for two conducting phases, *Earth planet. Sci. Lett.,* **180,** 369–383.

Hackney, R.I. *et al.*, 2006. The segmented overriding plate and coupling at the South-Central Chilean Margin (36–42°S), in *The Andes—Active Subduction Orogeny*, pp. 355–374. eds Oncken, O. *et al.*, Springer-Verlag.

Hamza, V.M. & Muñoz, M., 1996. Heat flow map of South America, *Geothermics,* **25**(6), 599–646.

Hansen, P.C. & O'Leary, D.P., 1993. The use of the L-Curve in the regularization of discrete ill-posed problems, *SIAM J. Sci. Comput.,* **14**(6), 1487–1503.

Held, S., Schill, E., Sanchez, P., Neumann, T., Emmerich, K., Morata, D. & Kohl, T., 2015. Geological and tectonic settings preventing high-temperature geothermal reservoir development at Mt. Villarrica (Southern Volcanic Zone): clay mineralogy and sulfate-isotope geothermometry, in *Proceedings World Geothermal Congress 2015,* Melbourne, Australia.

Hervé, F., 1976. Estudio geológico de la falla Liquñe-Reloncaví en el área de Liquñe; antecedentes de un movimiento tran- scurrente (Provincia de Valdivia), *Congr. Geol. Chil. Actas,* **1,** B39–B56.

Hervé, F., 1984. Rejuvenecimientode edades radiométricas y el sistema de fallas Liquiñe-Ofqui, *Comunicaciones,* **35,** 107–116.

Hickey-Vargas, R., Moreno-Roa, H., Lopez-Escobar, L. & Frey, F., 1989. Geochemical variations in Andean basaltic and silicic lavas from the Villarrica-Lanín volcanic chain (39.5°S): an evaluation of source heterogeneity, fractional crystallization and crustal assimilation, *Contrib. Mineral. Petrol.,* **103**(3), 361–386.

Hickey-Vargas, R., Sun, M., López-Escobar, L., Moreno-Roa, H., Reagan, M.K., Morris, J.D. & Ryan, J.G., 2014. Multiple subduction components in the mantle wedge: evidence from eruptive centers in the Central Southern volcanic zone, Chile, *Geology,* **30**(3), 199–202.

Hildreth, W. & Moorbath, S., 1988. Crustal contributions to arc magmatism in the Andes of Central Chile, *Contrib. Mineral. Petrol.,* **98,** 455–489.

Hill, G.J., Caldwell, T.G., Heise, W., Chertkoff, D.G., Bibby, H.M., Burgess, M.K., Cull, J.P. & Cas, R.A.F., 2009. Distribution of melt beneath Mount St Helens and Mount Adams inferred from magnetotelluric data, *Nat. Geosci.,* **2**(11), 785–789.

Hochstein, M.P. & Regenauer-Lieb, K., 1998. Heat generation associated with collision of two plates: the Himalayan geothermal belt, *J. Volcanol. Geotherm. Res.,* **83**(1–2), 75–92.

Ivanov, S.N. & Ivanov, K.S., 1994. Hydrodynamic zoning of the Earth's crust and its significance, *J. Geodyn.,* **17**(4), 155–180.

Jiracek, G.R., 1995. Geoelectromagnetics charges on, *Rev. Geophys.,* **33**(Issue S1), 169–176.

Jödicke, H., 1992. Water and graphite in the Earth's crust—an approach to interpretations of conductivity models, *Surv. Geophys.,* **13,** 381–407.

Jones, A.G., 1992. Electrical conductivity of the continental lower crust, in *The Continental Lower Crust*, pp. 81–143, eds Fountain, D.M., Arculus, R.J. & Kay, R.W., Elsevier.

Jordan, T.E., Burns, W.M., Veiga, R., Pángaro, F., Copeland, P., Kelly, S. & Mpodozis, C., 2001. Extension and basin formation in the southern Andes caused by increased convergence rate: a mid-Cenozoic trigger for the Andes, *Tectonics,* **20**(3), 308–324.

Kapinos, G., Montahaei, M., Meqbel, N. & Brasse, H., 2016. Three-dimensional electrical resistivity image of the South-Central Chilean subduction zone, *Tectonophysics,* **666,** 76–89.

Kohl, T. & Rybach, L., 1996. Thermal and hydraulic aspects of the KTB drill site, *Geophys. J. Int.,* **124,** 756–776.

Korja, T., Smirnov, M., Pedersen, L.B. & Gharibi, M., 2008. Structure of the central Scandinavian caledonides and the underlying precambrian basement, new constraints from magnetotellurics, *Geophys. J. Int.,* **175,** 55–69.

Krawczyk, C.M. *et al.*, 2006. Geophysical signatures and active tectonics at the South-Central Chilean Margin, in *The Andes—Active Subduction Orogeny*, pp. 172–192, eds Oncken, O. *et al.*, Springer.

Lange, D., Cembrano, J., Rietbrock, A., Haberland, C., Dahm, T. & Bataille, K., 2008. First seismic record for intra-arc strike-slip tectonics along the Liquiñe-Ofqui fault zone at the obliquely convergent plate margin of the southern Andes, *Tectonophysics,* **455,** 14–24.

Lara, L.E., 2004. Villarrica-Lanín chain: tectonic constraints for volcanism in a transversal alignment, *Boletín-Servicio Nacional de Geología y Minería,* **61,** 13–16.

Lara, L.E. & Moreno, H., 2004. *Geología del Área Liquine-Neltume*, Carta Geológica de Chile - Servicio Nacional de Geológia y Minería.

Lavenu, A. & Cembrano, J., 1999. Compressional- and transpressional-stress pattern for Pliocene and Quaternary brittle deformation in fore arc and intra-arc zones (Andes of Central and Southern Chile), *J. Struct. Geol.,* **21,** 1669–1691.

Lebedev, E.B. & Khitarov, N.I., 1964. Dependence on the beginning of melting of granite and the electrical conductivity of its melt on highwater vapor pressure, *Geochem. Int.,* **1,** 193–197.

Mackie, R.L., Livelybrooks, D.W., Madden, R. & Larsen, C., 1997. A magnetotelluric investigation of the San Andreas fault at Carrizo Plain, California, *Geophys. Res. Lett.,* **24**(15), 1847–1850.

Melnick, D. & Echtler, H.P., 2006. Inversion of forearc basins in south-central Chile caused by rapid glacial age trench fill, *Geology,* **34**(9), 709–712.

Melnick, D., Rosenau, M., Folguera, A. & Echtler, H., 2006. Neogene tectonic evolution of the Neuquén Andes western flank, *Geol Soc. Am. Spec. Pap.,* **407,** 73–95.

Moreno, H. & Lara, L.E., 2008. *Geología de Àrea Pucón-Curarrehue*, Carta Geológica de Chile - Servicio Nacional de Geológia y Mineria.

Moreno, H., Clavero, J. & Lara, L.E., 1994. Actividad explosiva postglacial de volcan Villarrica, Andes del sur, 39°25′S, in *Actas 7th Congreso Geologico Chileno*, pp. 329–333, Concepción, Chile.

Munizaga, F., Herve, F., Drake, R., Pankhurst, R.J., Brook, M. & Snelling, N., 1988. Geochronology of the Lake Region of south-central Chile (39°–42°S): preliminary results, *J. South Am. Earth Sci.,* **1**(3), 309–316.

Muñoz, M., Fournier, H., Mamani, M., Febrer, J., Borzotta, E. & Maidana, A., 1990. A comparative study of results obtained in magnetotelluric deep soundings in Villarrica active volcano zone (Chile) with gravity investigations, distribution of earthquake foci, heat flow empirical relationships, isotopic geochemistry 87Sr/86Sr and SB sys, *Phys. Earth planet. Inter.,* **60,** 195–211.

Niemeyer, H. & Muñoz, J., 1983. *Hoja Laguna de la Laja, Region del Bío Bío. Carta Geología de Chile 57,* Servicio Nacional de Geología y Minería.

Norabuena, E., 1998. Space geodetic observations of Nazca-South America convergence across the central Andes, *Science,* **279,** 358–362.

Ortiz, R., 2003. Villarrica volcano (Chile): characteristics of the volcanic tremor and forecasting of small explosions by means of a material failure method, *J. Volcanol. Geotherm. Res.,* **128**(1–3), 247–259.

OVDAS, 2015. Observatorio Volcanológico de los Andes del Sur: La Araucanía - Los Ríos, Report: 25.03.2015.

Pankhurst, R.J., Weaver, S.D., Hervé, F. & Larrondo, P., 1999. Mesozoic—Cenozoic evolution of the North Patagonian Batholith in Aysén, Southern Chile, *J. geol. Soc. Lond.,* **156,** 673–694.

Parda-Casas, F. & Molnar, P., 1987. Relative motion of the Nazca (Farallon) and South American plates since late cretaceous time, *Tectonics,* **6**(3), 233–248.

Radic, J.P., 2010. Las cuencas cenozoicas y su control en el volcanismo de los Complejos Nevados de Chillán y Copahue-Callaqui (Andes del Sur, 36–39°S), *Andean Geol*., **37**(1), 220–246.

Rapela, C.W. & Pankhurst, R.J., 1992. The granites of northern Patagonia and the Gastre Fault System in relation to the break-up of Gondwana, *Geol. Soc., Lond., Spec. Publ.,* **68**(1), 209–220.

Rodi, W. & Mackie, R.L., 2001. Nonlinear conjugate gradients algorithm for 2-D magnetotelluric inversion, *Geophysics,* **66**(1), 174.

Rosenau, M., Melnick, D. & Echtler, H., 2006. Kinematic constraints on intra-arc shear and strain partitioning in the southern Andes between 38°S and 42°S latitude, *Tectonics,* **25**(4), 1–16.

Rowland, J.V. & Sibson, R.H., 2004. Structural controls on hydrothermal flow in a segmented rift system, Taupo Volcanic Zone, New Zealand, *Geofluids,* **4,** 259–283.

Sánchez, P., Pérez-Flores, P., Arancibia, G., Cembrano, J. & Reich, M., 2013. Crustal deformation effects on the chemical evolution of geothermal systems: the intra-arc Liquiñe–Ofqui fault system, Southern Andes, *Int. Geol. Rev.,* **55**(11), 1384–1400.

Schill, E., Appel, E., Crouzet, C., Gautam, P., Wehland, F. & Staiger, M., 2004. Oroclinal bending versus regional significant clockwise rotations in the Himalayan arc—constraints from secondary pyrrhotite remanences, *Bull. geol. Soc. Am. Spec. Pap.,* **383,** 73–85.

Sibson, R.H., 1977. Fault rocks and fault mechanisms, *J. geol. Soc.,* **133**(3), 191–213.

Somoza, R., 1998. Updated Nazca (Farallon) -South America relative motions during the last 40 My: implications for mountain building in the central Andean region, *J. South Am. Earth Sci.,* **11**(3), 211–215.

Spichak, V., Geiermann, J., Zakharova, O., Calcagno, P., Genter, A. & Schill, E., 2015. Estimating deep temperatures in the Soultz-sous-Forêts geothermal area (France) from magnetotelluric data, *Near Surf. Geophys.,* **13**(4), 397–408.

Stern, C.R., 2004. Active Andean volcanism: its geologic and tectonic setting, *Andean Geol*., **31**(2), 161–206.

Suarez, M. & Emparan, C., 1995. The stratigraphy, geochronology and paleophysiography of a Miocene fresh-water interarc basin, southern Chile, *J. South Am. Earth Sci.,* **8**(1), 17–31.

Swift, C.M., 1967. *A Magnetotelluric Investigation of an Electrical Conductivity Anomaly in the Southwestern United States,* M.I.T.

ten Grotenhuis, S.M., Drury, M.R., Spiers, C.J. & Peach, C.J., 2005. Melt distribution in olivine rocks based on electrical conductivity measurements, *J. geophys. Res.,* **110**(12), 1–11.

Türkoğlu, E., Unsworth, M., Bulut, F. & Çağlar, İ., 2015. Crustal structure of the North Anatolian and East Anatolian fault systems from magnetotelluric data, *Phys. Earth planet. Inter.,* **241,** 1–14.

Tyburczy, J.A. & Waff, H.S., 1983. Electrical conductivity of molten basalt and andesite to 25 kilobars pressure: geophysical significance and implications for charge transport and melt structure, *J. geophys. Res.,* **88**(B3), 2413–2430.

Unsworth, M. *et al.*, 2004. Crustal and upper mantle structure of northern Tibet imaged with magnetotelluric data. *J. geophys. Res.,* **109**(B2), 1–18.

Unsworth, M.J., Malin, P.E., Egbert, G.D. & Booker, J.R., 1997. Internal structure of the San Andreas fault at Parkfield, California, *Geology,* **25**(4), 359–362.

Unsworth, M.J., Egbert, G.D. & Booker, J.R., 1999. High-resolution electromagnetic imaging of the San Andreas fault in Central Clifornia, *J. geophys. Res.,* **104**(B1), 1131–1150.

Unsworth, M.J. *et al.*, 2005. Crustal rheology of the Himalaya and Southern Tibet inferred from magnetotelluric data, *Nature,* **438**(7064), 78–81.

Wannamaker, P.E., Jiracek, G.R., Stodt, J.A., Caldwell, T.G., Gonzalez, V.M., McKnight, J.D. & Porter, A.D., 2002. Fluid generation and pathways

beneath an active compressional orogen, the New Zealand Southern Alps, inferred from magnetotelluric data, *J. geophys. Res.,* **107**(B6), 1–21.

Wannamaker, P.E., Evans, R.L., Bedrosian, P.A., Unsworth, M.J., Maris, V. & Shane McGary, R., 2014. Segmentation of plate coupling, fate of subduction fluids, and modes of arc magmatism in Cascadia, inferred from magnetotelluric resistivity, *Geochem. Geophys. Geosyst.* **15,** 4230–4253.

Waxman, M.H. & Smits, L.J.M., 1968. Electrical conductivities in oil-bearing shaly sands, *Soc. Petrol. Eng. J.,* **8,** 107–122.

Weckmann, U., Ritter, O., Chen, X., Tietze, K. & de Wit, M., 2012. Magnetotelluric image linked to surface geology across the Cape Fold Belt, South Africa, *Terra Nova,* **24**(3), 207–212.

Wiese, H., 1962. Geomagnetische Tiefentelluric Teil II: Die Streichrichtung der Untergrundstrukturen des elektrischen Widerstandes, erschlossen aus geomagnetischen Variationen, *Pure appl. Geophys.,* **52,** 83–103.

Zaffarana, C.B., López de luchi, M.G., Somoza, R., Mercader, R., Giacosa, R. & Martino, R.D., 2010. Anisotropy of magnetic susceptibility study in two classical localities of the Gastre Fault System, central Patagonia, *J. South Am. Earth Sci.,* **30**(3–4), 151–166.

Zhang, L. *et al.*, 2015. Structure of the Central Altyn Tagh Fault revealed by magnetotelluric data: new insights into the structure of the northern margin of the India–Asia collision, *Earth planet. Sci. Lett.,* **415,** 67–79.

SUPPORTING INFORMATION

Additional Supporting Information may be found in the online version of this paper:

Supplementary_Material.pdf
(http://gji.oxfordjournals.org/lookup/suppl/doi:10.1093/gji/ggw338/-/DC1).

Please note: Oxford University Press is not responsible for the content or functionality of any supporting materials supplied by the authors. Any queries (other than missing material) should be directed to the corresponding author for the paper.